Time-resolved x-ray emission spectra from optically ionized helium and neon plasmas

T. E. Glover,[1] J. K. Crane,[2] M. D. Perry,[2] R. W. Lee,[2] and R. W. Falcone[3]
[1]*Ernest Orlando Lawrence Berkeley National Laboratory, Berkeley, California 94720*
[2]*Lawrence Livermore National Laboratory, Livermore, California 94550*
[3]*Department of Physics, University of California at Berkeley, Berkeley, California 94720*
(Received 3 February 1997)

The interaction of high-power, subpicosecond laser pulses with gas targets is expected to produce highly nonequilibrium plasmas whose parameters are controlled by the laser wavelength and polarization. We investigate such plasmas by measuring time-resolved x-ray-emission spectra in highly ionized helium and neon plasmas produced by high-power optical ionization. Electron temperatures are observed to increase with increasing laser wavelength and with variation of the laser polarization from linear to circular. These results are in qualitative agreement with current models for production of tunnel-ionized laser plasmas. Limited quantitative agreement, however, reflects the complexity of the optical ionization process and suggests the important role rapid cooling processes can play in these plasmas. Emission spectra are combined with time-dependent kinetic simulations to assess prospects for x-ray lasers pumped by rapid electron-ion recombination.
[S1063-651X(97)10812-1]

PACS number(s): 52.40.Nk, 52.25.Nr, 42.55.Vc

I. INTRODUCTION

Recent advances in high-power, short-pulse laser technology permit experiments where atoms are briefly (10^{-12}–10^{-14} s) exposed to electric fields comparable to an atomic unit of field strength ($\sim 5\times 10^{11}$ V/m). A significant consequence for both plasma and atomic physics is the production and control of ''novel'' plasmas. ''Conventional'' (long pulse, e.g., nanosecond) laser plasmas achieve a high stage of ionization as ''seed'' electrons produced and heated by the laser collisionally ionize the medium; accordingly, the electron temperature is correlated with the ionization state of the plasma. In contrast, it has been proposed that intense, subpicosecond laser pulses can produce plasmas whose electron temperature and ionization state are, to a large extent, (i) decoupled from one another and (ii) independently controlled by laser parameters [1]. This decoupling between electron temperature and ion stage occurs since the ion stage is determined by the laser intensity while the electron temperature is determined by laser-electron interactions subsequent to ionization. If sufficiently short laser pulses are used, electron heating due to plasma wave generation or inverse bremsstrahlung absorption can be minimized and the electron temperature is determined by the (essentially single-atom) physics of the optical ionization process. In this process, commonly modeled as an electron tunneling through a laser-suppressed Coulomb barrier, the dominant factors determining the electron energy are the laser wavelength and polarization [1,2]. The ability to exercise fine control over plasma parameters is of interest both intrinsically and for applications ranging from x-ray laser generation [3] to creation of laser-plasma particle accelerators [4].

Leemans *et al.* have studied tunnel-ionized plasmas produced in the long-pulse (~ 500 ps), long-wavelength (10 μm) regime [5]; electron temperatures were observed to vary with laser polarization and were estimated to be of order 10 times higher than the ionization potential of the target gas sample. In contrast, proposals for using tunnel-ionized plasmas as x-ray lasing media are based on predictions that shorter-wavelength and shorter-duration laser pulses can generate electron temperatures comparable to (or significantly less than) the ionization potential of target gas [1–3]. Previous experiments performed with shorter-wavelength, subpicosecond laser pulses have utilized Thomson scattering to measure electron temperatures [6,7]. Thomson scattering experiments performed in our laboratory [6] indicate that average electron energies in tunnel-ionized He plasmas are well described by the so-called quasistatic model of Refs. [1–3]. The Thomson scattering experiments of Blyth *et al.* indicate that heating due to stimulated Raman scattering and inverse bremsstrahlung (IB) absorption become dominant at high gas density and high laser intensity [7]. Neither the work of Leemans *et al.* [5] nor the Thomson scattering measurements of [6,7] provides data on the *distribution* of electron energies in tunnel-ionized plasmas. Such information is important both for a basic understanding of the plasma generation mechanisms and for x-ray laser applications. The spectrum of free-bound plasma fluorescence can provide a direct mapping of the distribution of electron energies within a plasma, thus providing important complimentary data to the work of Refs. [5–7].

In this work time-resolved free-bound (and bound-bound) x-ray-emission spectra are measured from plasmas produced through the interaction of intense, subpicosecond laser pulses with helium and neon gas targets. Previously, we reported on results obtained using linearly polarized laser pulses and with helium gas samples [8]. Here we extend those measurements to study neon plasmas and to study the effects of laser polarization and wavelength.

The He experiments are performed at lower gas density and lower laser intensity than are the Ne experiments. The plasma parameters are primarily determined by the (atomic) ionization process. Evolution of the emission spectra occurs on a time scale comparable to the time resolution of the detection apparatus; we are able to resolve thermalization of the electron distribution as well as a cascade of population to

the ground state of He II. In addition, spectra are measured as a function of laser polarization. In qualitative agreement with the quasistatic model, heating of the electron distribution is observed as the laser polarization is varied from linear to circular. The initial distribution of electron energies, however, is not well described by this model. We discuss possible causes of the discrepancy. Electron-ion recombination is observed to proceed too slowly to produce (recombination) gain on the Lyman-α transition of He II. Measurement of the electron thermalization process, however, indicates that a Lyman-α laser (at 304 Å) with gain of order 10 cm^{-1} is feasible if a second laser pulse is used after thermalization of the electron distribution.

The Ne experiments are performed at higher gas density, higher laser intensity, and with longer laser pulses than are the He experiments. Accordingly, the electron temperature is expected to be much higher than for the He experiments and post-ionization heating mechanisms such as inverse bremsstrahlung absorption are expected to strongly influence the initial electron temperature. Emission spectra are measured as a function of laser wavelength. While significant heating of the electron distribution is observed with increased laser wavelength (in qualitative agreement with the quasistatic model), measured initial temperatures are significantly lower than expected. A model of thermal conduction cooling suggests that significant cooling of the plasma occurs on a time scale comparable to the time resolution of the detection apparatus. In particular, the highly ionized He-like plasma at the center of the laser-gas interaction region cools to a temperature determined by the surrounding, colder plasma on a sub–10-ps time scale.

II. HELIUM EXPERIMENTS

A. Apparatus

He experiments were performed using an organic-dye–based laser system [9]. A 160-fs laser pulse centered at 616 nm is focused to a peak intensity of 1×10^{16} W/cm^2 using an 8.1-cm focal length off-axis-parabolic mirror. The focal spot (16 μm in diameter) was positioned 1 mm from the exit of a pulsed gas valve (Lasertechnics model LPV), which provides an output gas density of 10^{18} atoms cm^{-3} for our experimental parameters of 100-psi backing pressure and 1-mm gas valve orifice [10]. Recombination fluorescence is collected at an angle of 90° with respect to the laser propagation direction using a gold-coated curved mirror and focused onto the entrance slit of a grazing incidence, x-ray monochrometer. Entrance and exit slits of the scanning monochrometer were set to 1 mm, which provides a spectral resolution of 6 Å for the 1200-lines/mm diffraction grating used in these experiments. The spectrally resolved fluorescence is detected with a microchannel plate intensifier and time-resolved using time-correlated photon counting [11]. Corrections for the spectral response of the detection apparatus, while accounted for, are minimal (nominally a 15% effect [12]). The temporal impulse response of the apparatus was measured by frequency-doubling laser pulses in a 1-mm potassium dihydrogen phosphate crystal and sending the nominally 100-fs UV pulses directly into the detection apparatus. A histogram of photon arrival times was recorded, which indicated a response time of 60 ps [full width at half maximum (FWHM)]. Circularly polarized laser pulses were generated with use of a quarter wave plate and found to be better than 95% circularly polarized.

B. Overview of spectra

A sequence in the evolution of the recombination spectra can be observed for linear laser polarization in Fig. 1 and for circular polarization in Fig. 2. While a range of ion stages from He^{2+} to neutral He are produced owing to the spatial distribution of the focused laser pulse, data were taken in a spectral region that emphasizes recombination kinetics within the fully ionized region of the plasma. For instance, bound-bound transitions to the ground state of He II cover a spectral range 40.8–54.4 eV, while bound-bound transitions within He I contribute fluorescence at photon energies below 25 eV. *Free-bound* transitions to the ground state of He II fluoresce at photon energies beyond 54.4 eV, while free-bound transitions to He I or to excited states of He II would appear predominantly at lower energies and do not contribute to the spectra as seen by the absence of continuum signal below 54 eV [see Figs. 1(a) and 2(a)].

The data points of Figs. 1 and 2 each represent an average of 2050 laser shots and a five-point smoothing algorithm was applied to the spectra. Error bars, assigned as the rms average of multiple traces, are nominally $\pm10\%$. At early time (0–50 ps) the recombination spectra are dominated by free-bound emission as only a small fraction of electrons has recombined to He^{2+}. The initial free-bound spectra peak $\sim10-30$ eV beyond the He II continuum edge at 54.4 eV. In contrast, the free-bound spectrum for a Maxwellian distribution of electrons is expected to peak at the continuum edge [13] so that the spectra suggest initially non-Maxwellian distributions. The initial free-bound structure is not reproduced at higher photon energies in the spectrum and consequently is not a second-order spectrum of the diffraction grating. Later in time (150–200 ps) the structure in the free-bound spectra becomes less pronounced, indicative of free-electron thermalization, and electron-ion recombination leads to the appearance of line emission. At the latest time (350–400 ps) the free-bound spectra are peaked at the continuum edge, consistent with full thermalization of the electron distribution, and bound-bound dominates free-bound emission. We will focus on two aspects of the emission spectra: (i) the free-bound spectrum, which maps the electron distribution in the He^{2+} plasma, and (ii) line emission, which indicates population cascade time scales of importance for recombination x-ray lasers.

C. Free-bound spectra and electron energy distributions

The free-bound spectrum provides a direct mapping of the electron energy distribution function since radiative recombination between an electron and an ion results in emission of a photon whose energy is the sum of the free-electron energy and the (binding) energy of the state to which the electron recombines. To derive electron distributions from the free-bound spectra (photon energies greater than 54.4 eV), we correct for the spectral variation of both the monochrometer energy resolution and the (hydrogenic) radiative recombination cross section. We begin with a discussion of

the initial electron distributions. Importantly, we note that IB heating is insignificant (we calculate less than 2 eV of IB heating) so that the distributions are determined by the (essentially atomic) ionization process.

1. Initial electron energy distributions

(a) Free-bound structure. The initial electron energy distributions (obtained from Figs. 1 and 2) are shown in Figs. 3(a) and 4(a) along with least-squares fits to Maxwellian distributions. Since the distributions exhibit a structure not expected for a Maxwellian distribution, we discuss possible

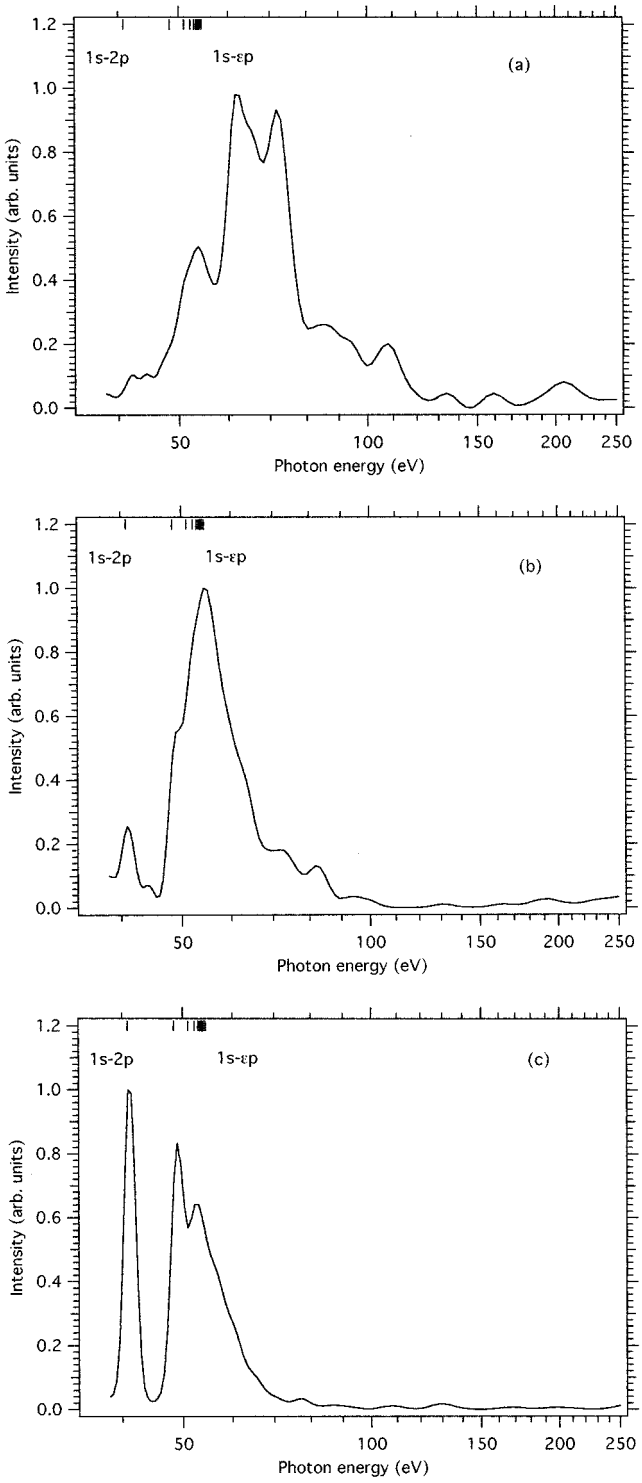

FIG. 1. Emission spectra from the He^{2+} plasma at times corresponding to (a) 0–50 ps, (b) 150–200 ps, and (c) 350–400 ps. Linearly polarized laser pulse were used (160 fs, 616 nm). Also shown are regions of line emission in He II. Free-bound emission corresponds to photon energies greater than 54.4 eV.

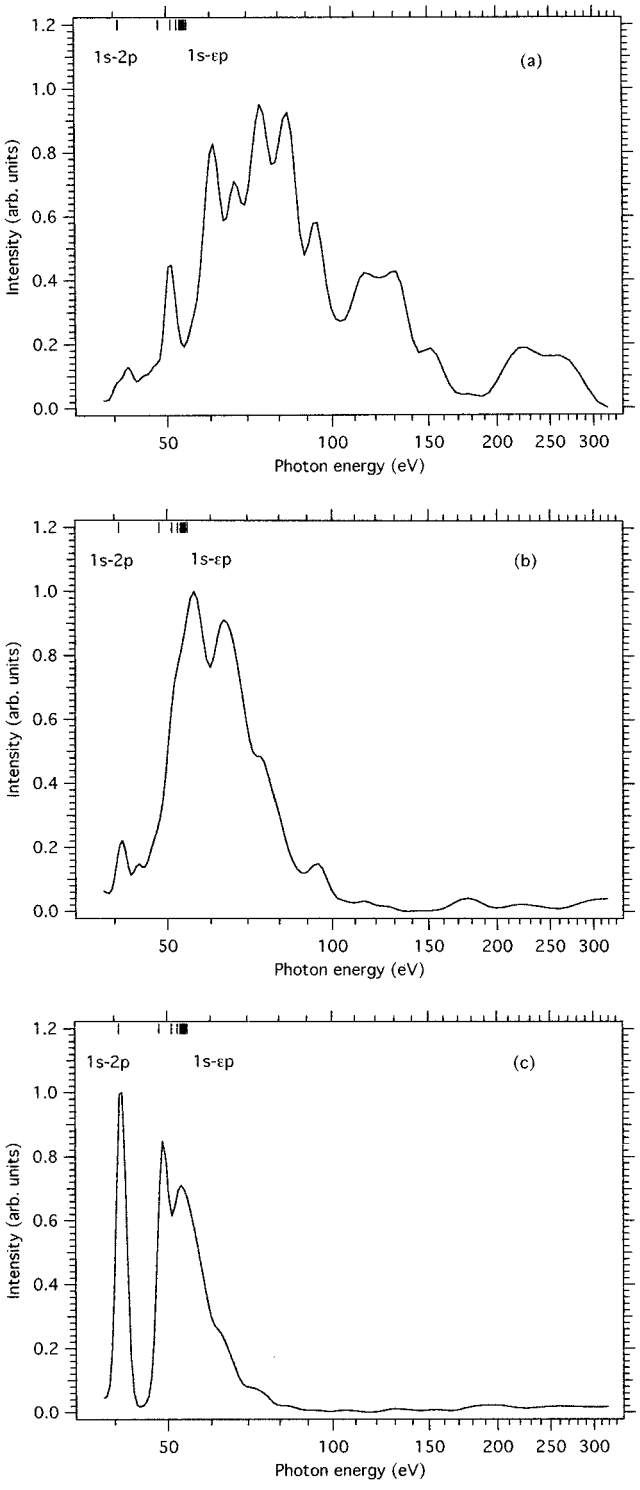

FIG. 2. Emission spectra from the He^{2+} plasma at times corresponding to (a) 0–50 ps, (b) 150–200 ps, and (c) 350–400 ps. Circularly polarized laser pulse were used (160 fs, 616 nm). Also shown are regions of line emission in He II. Free-bound emission corresponds to photon energies greater than 54.4 eV.

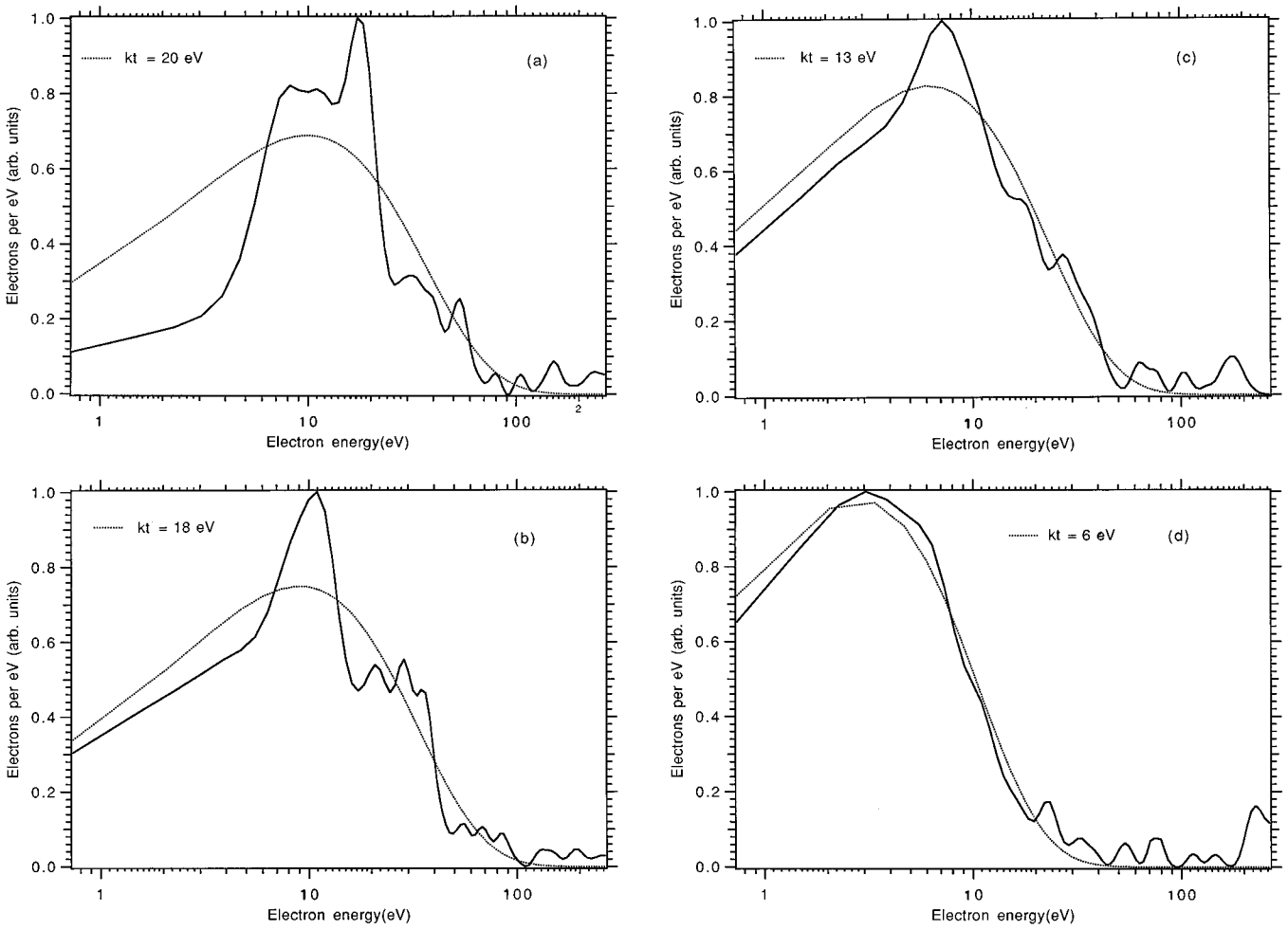

FIG. 3. Electron energy distributions within the He^{2+} plasma at times (a) 0–50 ps, (b) 50–100 ps, (c) 100–150 ps, and (d) 350–400 ps. Linearly polarized laser pulses were used. Energy distributions were obtained from the free-bound emission spectra as described in the text. Also shown are least-squares fits to Maxwellian distributions.

causes for the structure. Non-Maxwellian electrons could produce a structure in the free-bound continuum region as could fluorescence from doubly excited states with both electrons in states $n \geq 2$ [14]. However, three factors indicate that the observed structure cannot be attributed to fluorescence from doubly excited transitions. First, the doubly excited transitions that could potentially contribute to the observed features [Figs. 1(a) and 2(a) or Figs. 3(a) and 4(a)] involve two-electron transitions to the ground state of He I. These transitions are weak in comparison to single-electron transitions [14]; however, fluorescence from the accompanying single-electron transitions is not observed [see Fig. 1(a) near 40 eV]. This indicates that the structure above 60 eV [Figs. 1(a) and 2(a)] does not arise from two-electron transitions that occur after the laser pulse. Second, it is improbable that mixing of states by the laser could enhance the two-electron transition probability (in preference to the single-electron transition probability) sufficiently to cause appreciable fluorescence during the laser; the duty cycle of the 160-fs laser pulse is small compared to the 50-ps spectral integration time. Third, a similar structure previously has been observed in time-of-flight measurements of electron distributions resulting from high-intensity ionization of dilute He gas samples [15].

At this point it seems appropriate to place the initial spectra of Figs. 3(a) and 4(a) in the context of relevant models and related measurements. The optical ionization process responsible for plasma production is complex, involving nonperturbative atom-field interactions. However, it has been suggested that for sufficiently high laser intensity and long laser wavelength, the atom-field interaction can be treated quasiclassically [1,2] (the ''quasistatic'' limit). In this limit, ionization occurs as electrons tunnel through a (laser) suppressed Coulomb barrier; the free electron then interacts with a classical laser field. This quasistatic model has had some success in describing strong-field optical ionization and below we compare the measured spectra of Figs. 3(a) and 4(a) with quasistatic model predictions; where appropriate, closely related measurements are also discussed.

Ionization is calculated using the tunneling rates of Ammosov *et al.* [16] and by integrating over the temporal profile of the laser pulse at 100 points per optical cycle. We emphasize two considerations of interest from both a fundamental and an applications perspective: (i) the (initial) average electron energy and (ii) the form of the (initial) electron distribution.

(b) Average electron energy. The dilute gas measurements of Mohideen *et al.* [15] indicate that the quasistatic model

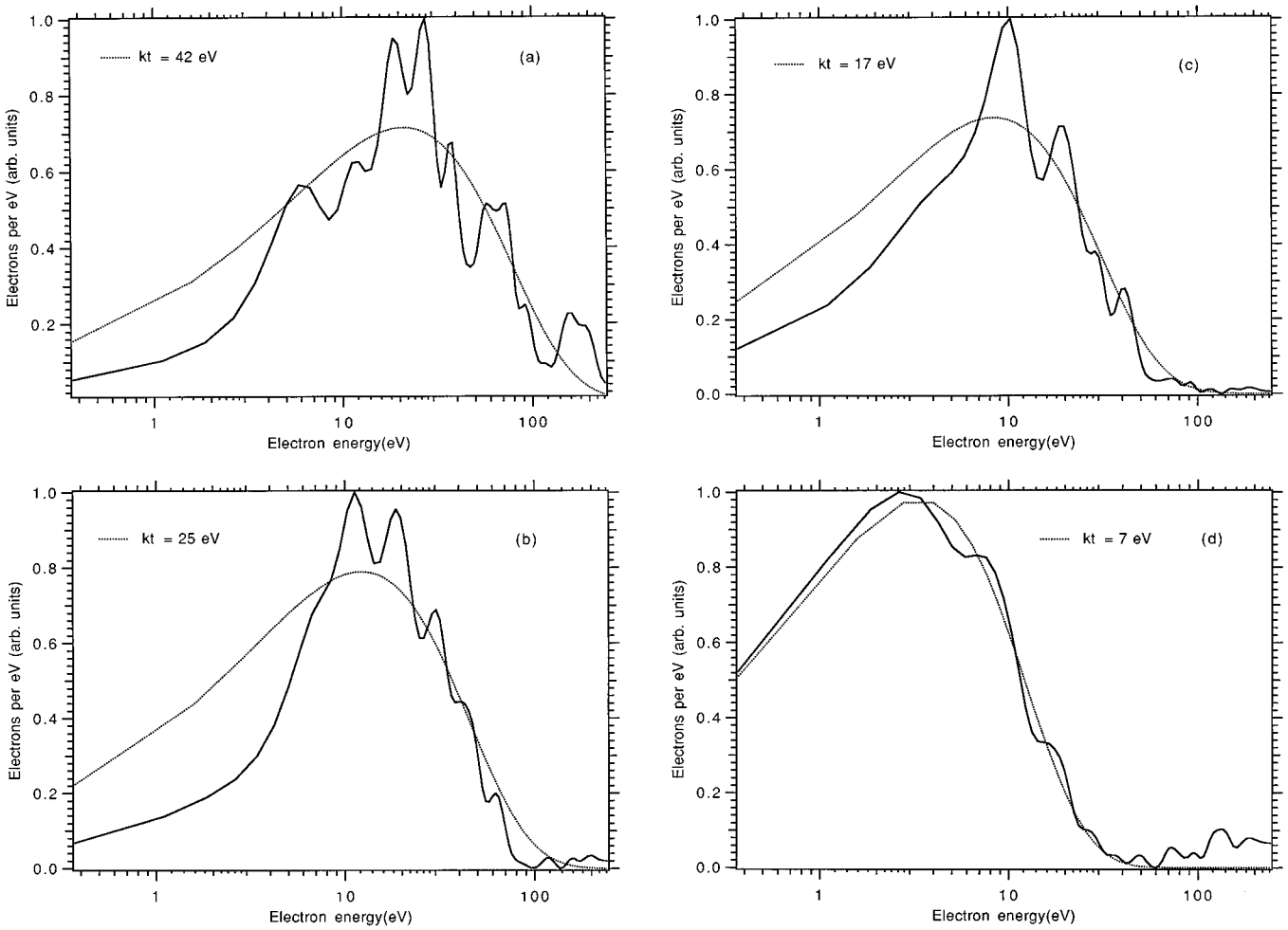

FIG. 4. Electron energy distributions within the He^{2+} plasma at times (a) 0–50 ps, (b) 50–100 ps, (c) 100–150 ps, and (d) 350–400 ps. Circularly polarized laser pulses were used. Energy distributions were obtained from the free-bound emission spectra as described in the text. Also shown are least-squares fits to Maxwellian distributions.

significantly underestimates the mean electron energy resulting from high power optical ionization of He. However, in a separate experiment, Thomson scattering measurements of high-density He gas samples indicate that average electron energies are well described by the quasistatic model [6]. The current (linear polarization) experiments are consistent with the Thomson scattering results: The average energy of the initial linear distribution (30 eV) is within 10% of the value predicted by the quasistatic model. The discrepancy between the dilute gas measurements of Mohideen *et al.* and the dense gas experiments of Ref. [6] could arise from two factors: (i) at high density collisional effects may modify the nascent electron distributions and (ii) the dilute gas experiments measured electron spectra along a specific direction, while the high-density experiments measured angle-integrated electron spectra.

When circular polarization is used, the initial average electron energy measured in the current work is 60 eV, approximately a factor of 3 lower than the average energy calculated from the quasistatic model. While some cooling has occurred over the time resolution of the measurement, the measured initial cooling rates (discussed below) suggest that the effects of cooling over the first time interval are small. The overestimation of average circular energies by the quasistatic model has also been observed by Mohideen *et al.* [15].

(c) Form of the initial electron distribution. We next discuss the form of the initial electron distribution. Neither the linear [Fig. 3(a)] nor the circular [Fig. 4(a)] distribution is well described by the quasistatic model, an observation consistent with previous measurements of (single-atom) electron distributions [15]. For instance, in contrast to the spectrum of Fig. 3(a), the quasistatic model predicts a linear electron distribution peaked at low ($\sim$1 eV) energy and a circular distribution with (approximately Gaussian) peaks at $\sim$80 and $\sim$500 eV.

Two factors may explain the departure from quasistatic distributions: (i) collisional effects and (ii) complexity of the optical ionization process. The important role electron-electron and electron-ion collisions play in restructuring the (single-atom) electron energy distribution has been emphasized by Ditmire [17] and Janulewicz, Grout, and Pert [18]. The modeling of Refs. [17] and [18] illustrates that single-atom calculations do not accurately describe electron distributions in even moderately dense (10^{18} cm^{-3}) plasmas: The narrow, cold quasistatic distributions are observed to broaden and to exhibit structure.

An additional complication arises from the potential complexity of the optical ionization process itself. The quasistatic model assumes ionization by a tunneling mechanism. In this regard we note that the Keldysh parameters [19] used to assess the appropriateness of tunneling ionization are 0.6 and 0.3 for single and double ionization of He, respectively. Since neither parameter is much smaller than unity, the ionization is expected to exhibit some character typical of multiphoton ionization (MPI) [20]. Accordingly, the nascent (single-atom) electron distribution will result from a number of factors known to be important for MPI such as above-threshold ionization, Stark-induced bound-state resonances, and shifts in the ionization potential of the atom or ion due to the ponderomotive potential of the laser [20]. It may be more accurate to characterize the ionization process as an interplay between multiphoton ionization and tunneling ionization. For instance, high-intensity MPI with subpicosecond lasers is known to be influenced by ionization through Stark-induced bound-state resonances involving Rydberg states [20]. At laser intensities above 10^{15} W/cm^2 an electron in such a Rydberg state will, rather quickly, be ionized via tunneling ionization. We stress that a proper treatment of the ionization process and ensuing (collisionally driven) evolution of the electron distribution is complex and remains an unsolved problem. We hope that the distributions of Figs. 3 and 4 can serve as guides for future simulations.

2. Evolution of the electron distribution

The evolution of the electron distributions can be observed in Figs. 3 and 4 [sequences (b)–(d)]. While the distributions are observed to thermalize at longer times, it is significant that the distributions do not thermalize in the $\sim$10-ps time scale necessary for peak gain in a He II $1s$-$2p$ recombination laser [21]. We note that thermalization is observed to occur in $\sim$200–300 ps for both laser polarizations. These thermalization time scales are in marked disagreement with the electron-electron collision time of $\sim$1 ps [22] for a Maxwellian distribution at our experimental parameters ($Z=2$, $kT=20$–40 eV, 10^{18} atoms cm^{-3}). Slow thermalization is consistent with an absence of cold electrons in the electron distribution since the electron-electron collision cross section is peaked for cold electrons [22].

The (temporal) evolution of the electron temperature is shown in Fig. 5 for both linear and circular polarization. At times when the distributions are nonthermal, equivalent ''temperatures'' have been defined as two-thirds of the average electron energy. The late-time linear and circular temperatures are comparable due to the larger thermal gradient inherent to the hotter distribution, which results in faster cooling. For instance, Fig. 5 indicates an initial linear cooling rate of 4 eV/50 ps and an initial circular cooling rate of 12 eV/50 ps. Both distributions cool to $\sim$5 eV in 300–400 ps.

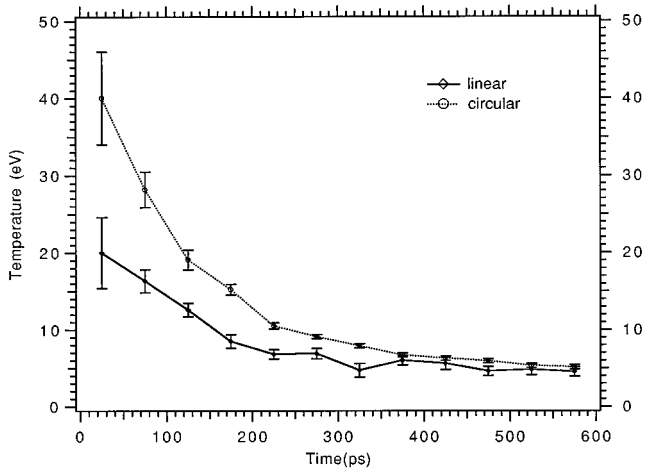

FIG. 5. Time-dependent electron temperatures in He^{2+} plasmas obtained using linearly and circularly polarized laser pulses. Experimental electron energy distributions not well approximated by a Maxwellian distribution have been assigned an equivalent ''temperature'' defined as two-thirds the average energy of the measured energy distribution function.

D. Line emission and x-ray laser implications

1. Population cascade time scale

Next we discuss the time evolution of the bound-state populations. The feasibility of recombination lasers is largely dependent upon a rapid cascade of population into the upper state of the lasing transition. Time-dependent fluorescence spectra allow us to assess whether such a cascade proceeds rapidly. In this context we note that the temporal evolution of $1s$-$2p$ line emission is indicative of the time scale on which appreciable population funnels into the $n=2$ state; this state is the upper level of a possible resonance line laser in He II [21]. Experimentally, we find that the $1s$-$2p$ transition dominates the recombination spectra at times later than 400 ps after the laser pulse. As discussed below, this time scale is approximately a factor of 100 slower than expected from simulations based on assumption of a Maxwellian distribution.

Calculations for gain in recombination lasers typically assume a Maxwellian distribution of electrons at a temperature estimated from the quasistatic model [3,21]. Using this assumption, we model our recombination spectra with the time-dependent recombination kinetics code FLY [23]. FLY considers bound-bound and bound-free processes within the plasma while also accounting for optical absorption affects. The density history of the plasma, as predicted by a model of adiabatic expansion [24,10] at an initial density of 10^{18} atoms cm^{-3}, was coupled to the measured (linear) temperature history to drive the calculations forward in time. The decay in electron density due to recombination is calculated self-consistently by the code and the predicted time-dependent spectra were convolved with the spectral response of the detection apparatus. We find that the $1s$-$2p$ transition in He II is predicted to dominate free-bound emission in 5 ps, approximately 100 times faster than measured. While this time scale is dependent on density, our results would not change qualitatively owing to uncertainty in the gas density. Simulations indicate that the gas density would have to be more than two orders of magnitude lower (than 10^{18} atoms cm^{-3}) to explain the discrepancy between our simulations and the initial spectrum of Fig. 1; the gas density is uncertain by nominally a factor of 4 [10].

The observed slow recombination is consistent with a free-electron distribution that exhibits a deficit of cold elec-

trons in comparison to a Maxwellian distribution. Qualitatively, the rise of $1s$-$2p$ line emission is expected to be slower given a deficit of cold electrons owing to the decreased cross sections for both three-body recombination and the ensuing collisional deexcitation cascade. We have integrated both the initial distribution of Fig. 3(a) and the associated best fit Maxwellian ($kT=20$ eV) over the three-body recombination and collisional deexcitation cross sections [25] and find that the three-body recombination rate for our measured distribution is a factor of 3 slower than expected for the Maxwellian, while collisional deexcitation rates are nominally 10% slower. Given this modification of collisional deexcitation rates, it is not a simple procedure to estimate the time scale for a population cascade to the $n=2$ state of He II. One must include all collisional processes as well as the inverse processes in a time-dependent fashion. This requires a recombination kinetics code that does not assume a Maxwellian distribution of electrons and is beyond the scope of the present work.

2. Gain using two laser pulses

Instead, we attempt to draw some conclusions as to the feasibility of recombination x-ray lasers (in He) given the present measurements. Pulsifer *et al.* have calculated gain on the Lyman-α transition of He II assuming a Maxwellian distribution of electrons [21]. The present work indicates that the population cascade to the upper lasing level is too slow to support gain. This result is consistent with the non-Maxwellian electron distribution observed at early time and suggests that the gain may be recovered by allowing the distribution to thermalize before electron-ion recombination establishes a population inversion. During the time required for thermalization the plasma will cool (favorable for gain) yet population will accumulate in the ground state of the lasing transition (unfavorable for gain). A second laser pulse could then be used to ionize this ground-state population. To assess the feasibility of this approach, three considerations are addressed.

First, during the thermalization time interval (300–400 ps) the electron and ion densities decay due to both electron-ion recombination and expansion of the plasma. To estimate the effects of plasmas expansion, we assume cylindrical, adiabatic expansion, which leads to the expression [24,10]

$$N(t+dt)=N(t)\{1/[1+dt/R(t)/V(t)]\}^2, \qquad (1)$$

where R is the plasma radius and V the expansion velocity (taken as the sound speed $\sqrt{ZkT_e/M_{\rm ion}}$). Using the measured (linear) temperature history and an initial radius of 8 μm, Eq. (1) indicates a reasonably mild 30% drop in density after 400 ps. To estimate the significance of electron-ion recombination we use the time-dependent code FLY. Again the measured temperature history drives the calculations forward in time and a range of initial gas densities from 1×10^{18} to 3×10^{19} cm^{-3} is assumed. For an initial atomic density of 10^{18} cm^{-3}, the fractional recombination at 400 ps is less than 2%. This increases to $\sim$40% for an initial density of 3×10^{19} cm^{-3}, with 5% of this recombined population in the ground state of the Lyman-α transition. Electron-ion recombination, therefore, can be classified as a minor (5%) effect. Reionization of the ground-state population will not constitute a significant perturbation of the free-electron bath. The remaining (35%) of recombined population resides in weakly bound states (binding energy less than 10 eV) and will lead to cold free electrons upon ionization by the second laser pulse.

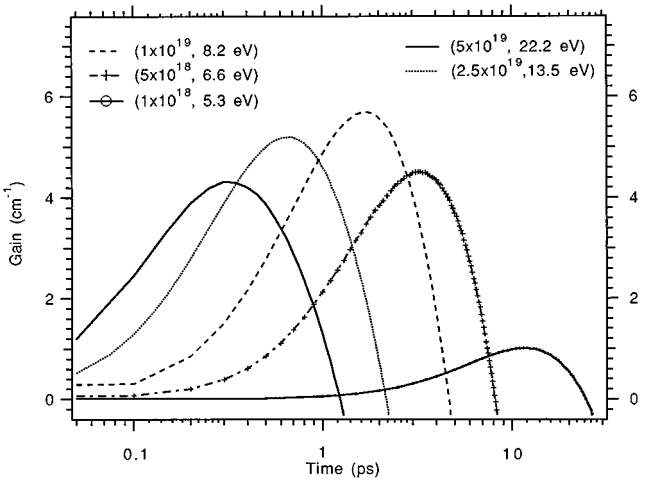

FIG. 6. Time-dependent gain curves for the Lyman-α transition in He II using the two-ionizing laser pulse scenario discussed in the text. Ion densities (cgs units) seen by the second laser pulse are shown, as are predicted electron temperatures (in eV). The electron temperatures result from inverse bremsstrahlung heating by the second laser pulse given a preformed plasma with an initial electron temperature of 5 eV.

Next we consider whether the second laser pulse significantly heats the existing bath of free electrons. We calculate IB heating using the heating rates of Jones and Lee, who provide analytic expressions (consistent with Monte Carlo simulations) for IB heating at low and high laser intensity [26]. For intermediate laser intensities we use a fourth-order polynomial fit to interpolate between the analytic expressions. We assume a laser pulse duration of 100 fs (FWHM), a peak intensity of 1×10^{16} W/cm^2, and an initial electron temperature of 5 eV. Effective temperatures are defined as two-thirds the energy gained by IB absorption. The electron temperature increases by $\sim$3 eV for an initial gas density of 10^{19} cm^{-3} and the heating varies approximately linearly with density. Heating by IB absorption is therefore moderate.

Finally, the Lyman-α gain is calculated using [21]

$$g\ \ (\mathrm{cm}^{-1})=(918.75)(T_e^{0.25}/N_e^{0.93})[N_2g_1/g_2-N_1], \qquad (2)$$

where T_e is the electron temperature in eV, N_e is the free-electron density in cgs units, and N_i and g_i are the population and degeneracy of the upper (2) and lower (1) states. FLY is used to determine the time-dependent bound-state populations. Time-dependent gain profiles are shown in Fig. 6 for several ion densities (as ''seen'' by the second laser pulse). An initial electron temperature of 5 eV is assumed and the final electron temperatures (after IB heating from the second 100-fs, 616-nm, 1×10^{16}-W/cm^2 laser pulse) are indicated in Fig. 6. Peak gains between 1 and 6 cm^{-1} are indicated, limited by IB heating. If current ultrashort laser pulses are used then the IB heating can be reduced. As an example, a 30-fs laser pulse from a state-of-the-art Ti:sapphire laser system

(800 nm) contributes less than 1 eV to the electron temperature given an initial density of 10^{19} cm^{-3}. Under these conditions we calculate a peak Lyman-α gain of 15 cm^{-1}. It therefore seems reasonable to conclude that the adverse affects of initial non-Maxwellian electron distributions can be avoided and that gain coefficients of order 10 cm^{-1} are feasible if two laser pulses are used. In this context, we note that a slightly different two-pulse scenario has been adopted by Nagata *et al.* in experiments on Li [3].

III. NEON EXPERIMENTS

A. Experimental apparatus

The neon experiments were performed using a 10-TW, Nd:glass laser system that provided either 800-fs pulses at 1.05 μm or 600-fs pulses at 526 nm [27]. The beams were focused with a 69-cm focal length aspheric lens to focal spot diameters of 42 and 22 μm (for 1-μm and 526-nm light, respectively). The beam energies were adjusted to produce a focused peak intensity of 5×10^{17} W/cm^2 in both cases. Laser pulses were sent into a vacuum chamber at a base pressure of 10^{-6} Torr and focused 1 mm from the exit of a supersonic pulsed gas valve, which provided a peak output gas density of 8×10^{18} atoms cm^{-3} [28]. Recombination fluorescence was collected with a point-to-point imaging, grazing incidence x-ray spectrometer (Hettrick Scientific Model HIREFS-SXR-1.75/SA-SB) and imaged onto the photocathode of an x-ray streak camera. The time resolution achieved in these experiments was limited by signal-to-noise considerations (i.e., signal level determined the fastest sweep speed used). A personal computer collected data from a cooled charge coupled device array, enabling collection of single-shot, spectrally and temporally resolved fluorescence spectra.

B. Overview of spectra and wavelength dependence

At the laser intensity used in these experiments, tunneling ionization rates [16] predict that greater than 99% of the Ne atoms at the center of the laser-gas interaction region will be ionized to Ne^{8+}, with less than 1% ionized to Ne^{9+}. The spectral range of the data is chosen to study the temperature history of this highly ionized He-like neon plasma. In particular, we focus on free-bound emission between electrons and He-like ions (which occurs for photon energies greater than 240 eV) while also observing bound-bound emission from Li-like ions.

The spatial distribution of the focused laser beam results in production of lower ion stages in the spatial wings of the laser focal spot; emission from these regions occurs predominantly at lower photon energies, outside the spectral window in which data were accumulated. The most significant contribution from lower ion stages is due to free-bound emission from the Ne^{7+} plasma (which may overlap free-bound emission from the Ne^{8+} plasma). Two factors minimize the effects of overlap. First, given the proximity of the Be-like continuum edge (207 eV) to the Li-like continuum edge (240 eV), the spatial volume that is ionized to Ne^{7+} (requiring the laser to overcome a 207-eV potential barrier) but not Ne^{8+} (a 240-eV potential barrier) is small (ratio of 1:5 by volume). Second, the Ne^{7+} and Ne^{8+} plasmas are expected to have roughly equivalent initial temperatures (since their ionization potentials are similar) so that overlap of the continua does not complicate matters. As further corroboration, we note that simulations using the kinetics code FLY indicate that line ratios from bound-bound emission in the Ne^{8+} plasma are consistent with temperatures determined from continuum slope measurements.

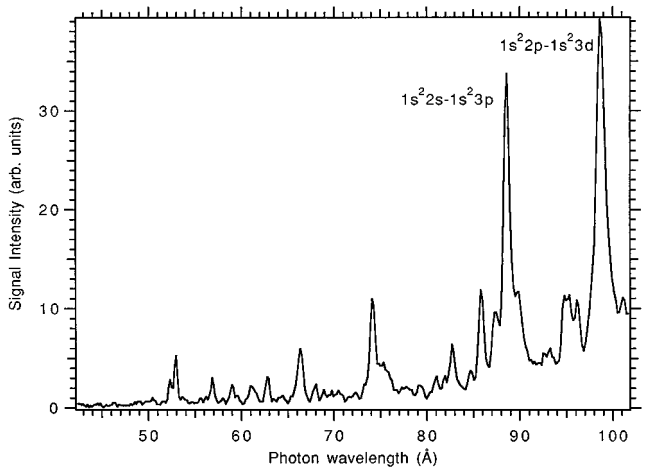

FIG. 7. Representative spectrum of electron-ion (radiative) recombination to the He-like Ne ion ($\lambda<52$ Å) and of line emission within the Li-like Ne ion ($\lambda>52$ Å). The spectrum is obtained using 526-nm, linearly polarized, 600-fs laser pulses. The prominent features near 98 and 88 Å are the $1s^2 2p$-$1s^2 3d$ and $1s^2 2s$-$1s^2 3p$ transitions, respectively, in Li-like Ne.

A representative emission spectrum integrated over 50 ps and obtained using 526-nm light is shown in Fig. 7. In contrast to the He experiments, line emission dominates free-bound emission at early time and free-bound emission is peaked at the continuum edge, indicative of a Maxwellian distribution. The $1s^2 2l$-$1s^2 nl'$ series in Li-like Ne is observed with the $1s^2 2p$-$1s^2 3d$ line at 98 Å predominant. We note that the 98-Å line has been proposed as a potential (recombination) x-ray lasing transition [3]. Also prominent are the $1s^2 2s$-$1s^2 3p$ (88-Å) and $1s^2 2p$-$1s^2 4d$ (74-Å) transitions.

The features appearing near 230 and 310 eV in the 1-μm spectra of Fig. 9 (discussed below) are higher-order diffraction features of the $1s^2$-$1s2p$ transition at 13.4 Å in Ne^{9+}. It has been proposed that this feature may arise from collisional excitation and ionization due to hot electrons created via stimulated Raman scattering [29].

C. Initial temperatures and wavelength dependence

A temporal sequence of emission spectra is shown in Fig. 8. Temperatures are determined from the slopes of the free-bound portions of the spectra, but are not precisely equal to these slopes [10,13]. A least-squares fit to the continuum region indicates an initial (0–50 ps) temperature of 41 eV. Cooling of the plasma is observed in the subsequent spectra. When the laser wavelength is increased, significant heating of the electrons is observed. Continuum emission resulting from 1-μm laser light is shown in Fig. 9 and the initial temperature is 136 eV, nominally a factor of 3 hotter than obtained with 526-nm light. The quasistatic model predicts a wavelength squared or factor of 4 increase.

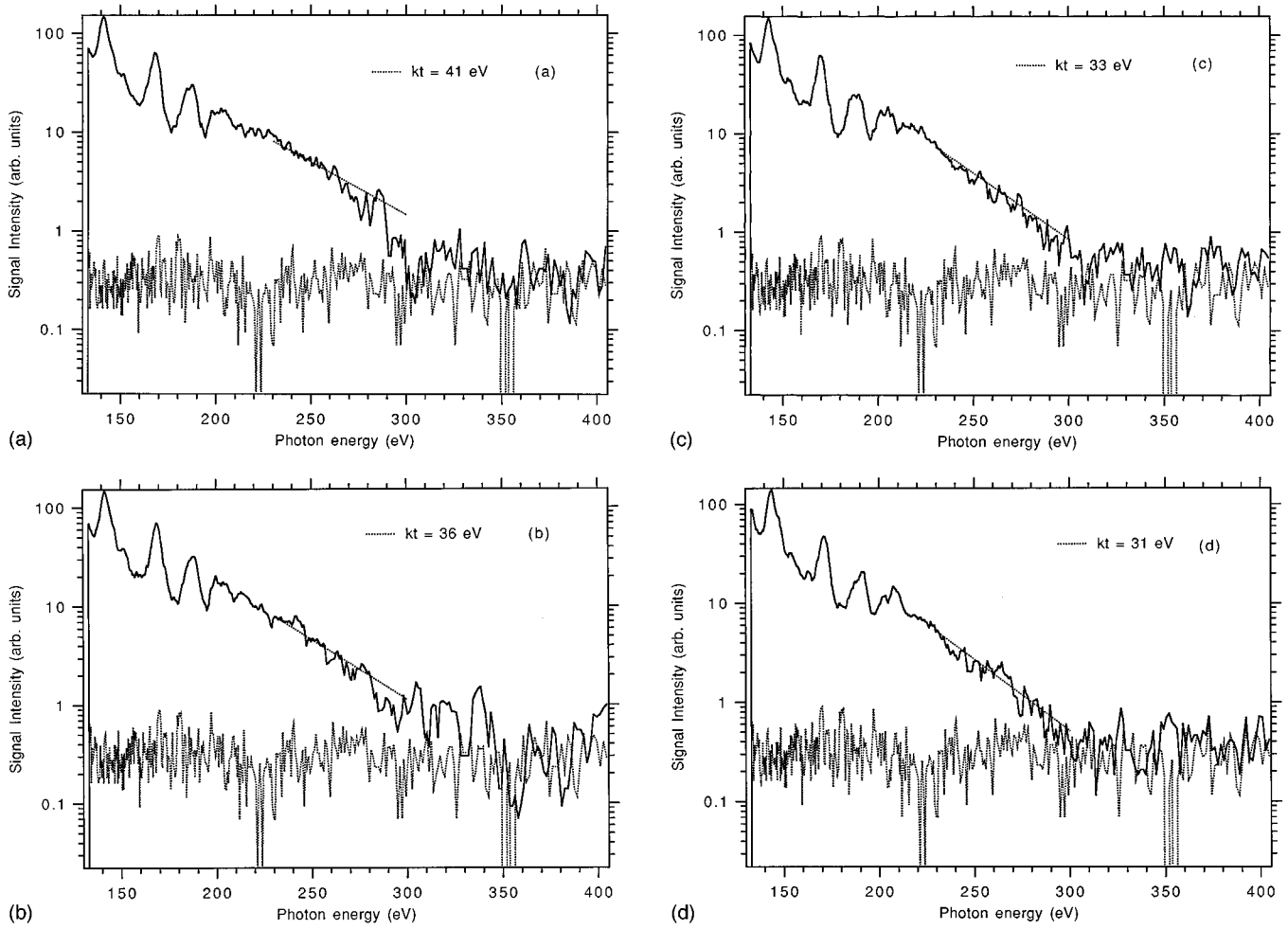

FIG. 8. Temporal sequence of free-bound emission spectra in the He-like Ne plasma at times corresponding to (a) 0–50 ps, (b) 300–350 ps, (c) 700–750 ps, and (d) 800–850 ps. Spectra were obtained using 526-nm laser light. Also shown are least-squares fits indicating electron temperatures in the Ne^{8+} plasma. The noise level of the detection apparatus is shown as a dashed line.

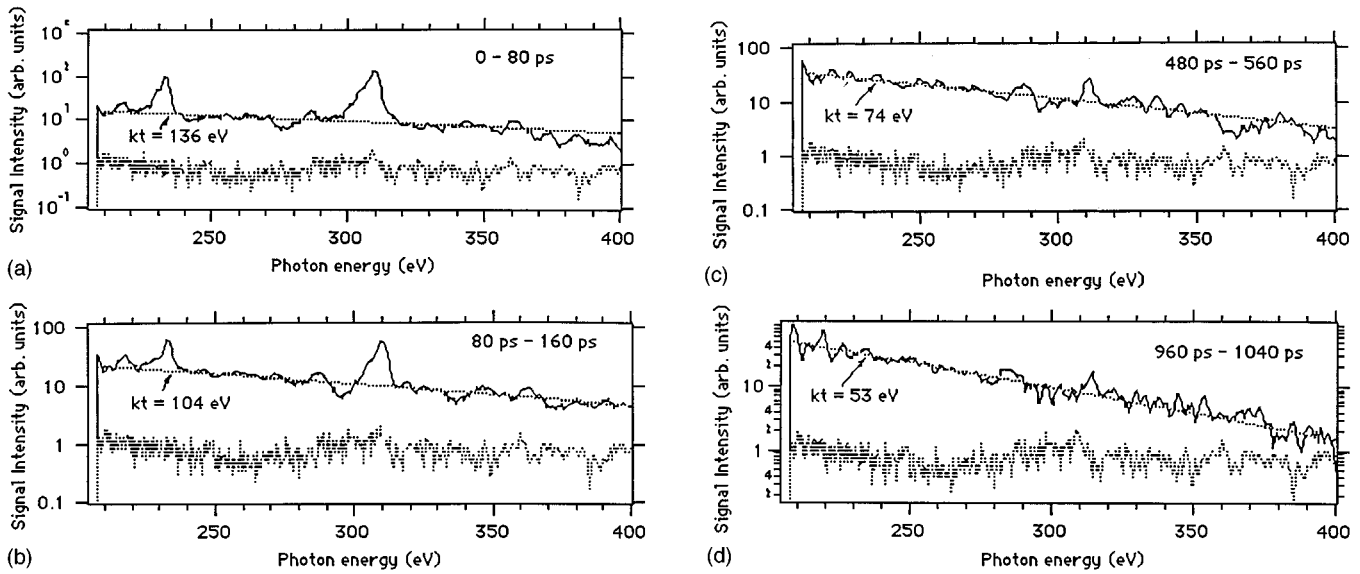

FIG. 9. Temporal sequence of free-bound emission spectra in the He-like Ne plasma at times corresponding to (a) 0–80 ps, (b) 80–160 ps, (c) 480–560 ps, and (d) 960–1040 ps. Spectra were obtained using 1-μm laser light. Also shown are least-squares fits indicating electron temperatures in the Ne^{8+} plasma. The noise level of the detection apparatus is shown as a dashed line.

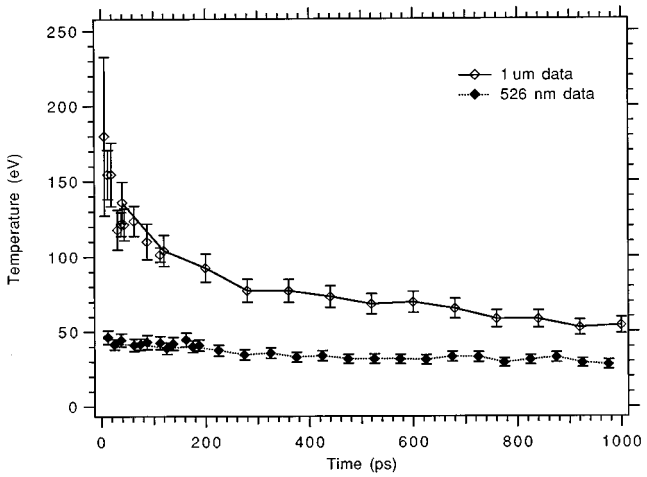

FIG. 10. History of electron temperatures in Ne^{8+} plasmas obtained using 526-nm and 1-μm laser light. Error bars are determined by the larger of either the shot-to-shot variation or the uncertainty in the least-squares fit to the continuum region.

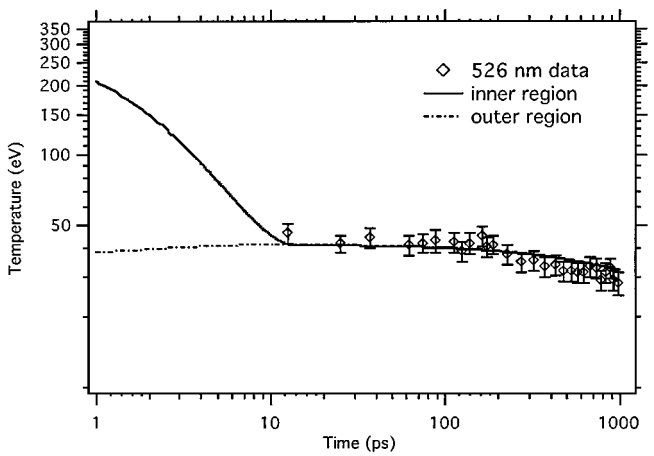

FIG. 11. Measured electron temperatures in the He-like Ne plasma obtained using 526-nm light. Also shown is the result of a thermal conduction cooling model discussed in the text. The inner (Ne^{8+}) plasma is shown to rapidly cool against the surrounding (outer) plasma at a lower stage of ionization.

Measured initial temperatures are significantly lower than expected. To predict an initial temperature we consider ionization heating and heating by IB absorption. The quasistatic model is used to calculate ionization heating. Electron distributions are calculated by integrating (at 100 points per optical cycle) the tunneling ionization rates of Ref. [16] over the temporal profile of the laser pulse and by accounting for ground-state depletion. The average energy resulting from eight sequential ionization events (to Ne^{8+}) is determined and effective temperatures are defined as two-thirds the average energy. Inverse bremsstrahlung absorption is calculated as described above using the heating rates of Ref. [26] and by accounting for time-dependent ionization over the temporal profile of the laser pulse. Using the above procedure and our experimental parameters, we calculate initial temperatures of 350 eV with 526-nm light and 760 eV with 1-μm light. While additional heating can be expected from stimulated Raman scattering (SRS), such a calculation is beyond the scope of the present work; the primary purpose of the calculations presented above is to illustrate that the measured temperatures are significantly lower than expected.

D. Cooling rates and rapid plasma cooling

Measured temperature histories (over the first nanosecond) are shown in Fig. 10 and average cooling rates are $\sim$15 eV/ns (526 nm) and $\sim$100 eV/ns (1 μm). Rapid initial cooling is observed with 1-μm light: The cooling rate over the first 10 ps is $\sim$1 keV/ns. While rapid initial cooling is not directly observed in the 526-nm data, we show below that the initial cooling may be unresolved.

To model the initial cooling process, we consider the 526-nm data since the (uncalculated) effects of SRS heating are expected to be less severe than for 1-μm light. We consider cooling by thermal conduction. When the mean-free electron-electron collision length is small compared to the plasma radius, a classical (diffusive) model of thermal conduction is appropriate [30]. In this regime we use the cooling coefficients of Spitzer [31]. If, on the other hand, the mean free-electron collision length is larger than one-tenth the plasma radius then thermal conduction is modeled as flux-limited free-streaming thermal conduction [30]. To account for the spatial profile of the focused laser beam, we divide the laser-gas interaction area into two regions: an inner region where Ne^{6+}, Ne^{7+}, and Ne^{8+} dominate and an outer region representing an average of the remaining ion stages. The inner region is heavily dominated by Ne^{8+} since we calculate that this ion is produced by the laser over a radius of 11 μm, while Ne^{7+} and Ne^{6+} are produced between 11 and 12 μm and 12 and 13 μm, respectively. We assign a volume weighted average temperature (of 315 eV) to this region determined by the predicted initial temperatures of ion stages $6+$, $7+$, and $8+$. Initial temperatures are calculated as described above. A similar procedure is used for the outer plasma region (the initial calculated temperature is 35 eV and the plasma radius is 120 μm).

Figure 11 shows the calculated temperature evolution of both the inner and outer plasma regions. Initially, free-streaming thermal conduction rapidly transports heat from the inner plasma to the surrounding (colder) plasma. Subsequent to this rapid initial cooling, the entire plasma cools by classical thermal conduction at a much slower rate (thermal gradients are smaller). The outer plasma thus acts as a thermal bath against which the inner plasma cools. The flux-limit parameter was set to 0.25 to produce the results of Fig. 11. If this adjustable parameter is increased then more rapid cooling results. The flux limiter is an essentially phenomenological parameter used to connect simple models of free-streaming thermal conduction to predictions from more sophisticated numerical models for heat transfer [30,32]. The model described above therefore only serves to illustrate the feasibility of an initial rapid cooling event and is not intended to quantitatively describe the initial rapid cooling or to make definite statements concerning the initial temperatures (which are unresolved). A sophisticated treatment of heat transfer in tunnel-ionized plasmas seems timely and our results should be taken as a data point against which such a calculation can be compared. Such a calculation is important from an applications perspective since very rapid cooling is required for recombination x-ray laser schemes: In Li-like Ne, for example, the $3d_{5/2}$-$2p_{3/2}$ (98-Å) gain lasts for less

than 1 ps, so the plasma must cool to ~40 eV in 1 ps [3]. We measure that this (40-eV) temperature is obtained in less than 10 ps, but signal and instrument considerations limit our ability to make direct measurements on a subpicosecond time scale.

IV. CONCLUSION

In conclusion, we have time-resolved the x-ray-emission spectra of plasmas produced by intense, subpicosecond laser pulses and find that control of the electron ''temperature'' is achieved with variation of either the laser wavelength or polarization. Helium experiments are performed in a parameter regime where the optical ionization process determines the initial distribution of electron energies. However, the measured initial distributions are not well described by the quasistatic model. We speculate that the discrepancy arises from a combination of two factors: (i) (collision driven) evolution of the electron distribution during the measurement interval and (ii) inability of the quasistatic model to correctly describe the initial electron distributions. Since the measured (linear) distribution exhibited fewer cold electrons than expected from either the quasistatic model or from a Maxwellian distribution with the same average energy, electron-ion recombination was observed to proceed significantly slower than expected. This slow recombination adversely affects prospects for recombination x-ray lasers and we calculate that plasma kinetics are sufficiently mild over the measured (electron) thermalization time that a gain of order 10 cm^{-1} is feasible for the Lyman-α transition of He II (304 Å) if two, time-delayed, laser pulses are used.

The Ne experiments are performed in a parameter regime where post-ionization heating strongly influences the initial electron temperature. Measured initial temperatures are much lower than expected and a model based on flux-limited free-streaming thermal conduction indicates that large thermal gradients result in rapid (initial) cooling rates. Efficient heat conduction therefore determines the electron temperature as observed on a 10-ps time scale: The highly ionized (hot) plasma at the center of the laser-gas interaction region cools to a temperature determined by the surrounding (colder) plasma at a lower stage of ionization. As to the form of the electron energy distribution, we observe Maxwellian distributions on a 10-ps time scale; the nascent distributions are unresolved. Further experiments and calculations are required to determine the initial distributions and cooling rates. In this context we note that recent developments in femtosecond x-ray measurement technology may permit measurement of x-ray-emission spectra with less than 100 fs time resolution [33].

ACKNOWLEDGMENTS

T.E.G. would like to thank AT&T for financial support. This work was also supported by the U.S. Air Force Office of Scientific Research and through a collaboration with Lawrence Livermore National Laboratory under Contract No. W-7405-ENG-48.

[1] R. R. Freeman *et al.*, Phys. Rev. Lett. **59**, 1092 (1987); N. H. Burnett and P. B. Corkum, J. Opt. Soc. Am. B **6**, 1195 (1989).

[2] P. B. Corkum, N. H. Burnett, and F. Brunel, Phys. Rev. Lett. **62**, 1259 (1989).

[3] N. H. Burnett and G. D. Enright, IEEE J. Quantum Electron. **26**, 1797 (1990); P. Amendt, D. C. Eder, and S. C. Wilks, Phys. Rev. Lett. **66**, 2589 (1991); D. C. Eder, P. Amendt, and S. C. Wilks, Phys. Rev. A **45**, 6761 (1992); Y. Nagata *et al.*, Phys. Rev. Lett. **71**, 3774 (1993); B. E. Lemoff *et al.*, *ibid.* **74**, 1574 (1995).

[4] T. Tajima and J. M. Dawson, Phys. Rev. Lett. **43**, 267 (1979); C. Joshi *et al.*, Nature (London) **311**, 525 (1984).

[5] W. P. Leemans *et al.*, Phys. Rev. Lett. **68**, 321 (1992); Phys. Rev. A **46**, 1091 (1992).

[6] T. E. Glover *et al.*, Phys. Rev. Lett. **73**, 78 (1994).

[7] W. J. Blyth *et al.*, Phys. Rev. Lett. **74**, 554 (1995).

[8] T. E. Glover *et al.*, Phys. Rev. Lett. **73**, 445 (1995).

[9] M. Murnane and R. W. Falcone, J. Opt. Soc. Am. B **5**, 1573 (1988).

[10] T. E. Glover, Ph.D. thesis, University of California at Berkeley, 1993 (available from University Microfilms Inc., 300 North Zeed Rd., Ann Arbor, MI 48106-1346).

[11] A general explanation of time-correlated photon counting can be found in, for instance, the Stanford Research Systems instrument catalog (application notes). In our application of the technique we work in a photon counting regime (~0.1 detected photons per laser shot) and proceed as follows: (i) a signal from the microchannel plate detector is sent to a constant fraction discriminator (CFD) (ORTEC model 934) and (ii) the signal from the CFD is sent to a time-to-amplitude converter (TAC) (ORTEC model 566). A (laser) photodiode signal triggers the TAC, which now waits for a signal from the CFD. When this signal is received (a photon is detected), the TAC outputs a voltage to indicate the time delay between the laser trigger and the detected photon. A personal computer reads the TAC voltage on every laser shot to determine if (and when) a photon was detected. As indicated in the text, frequency-doubled laser pulses (~100 fs) were used to determine the time resolution of the apparatus; we also note that the same laser pulses determine time zero for the experiment.

[12] We calculate that the spectral response of the detection apparatus varies by ~15% between 55 and 120 eV. Three factors are included in the calculation. First, the wavelength-dependent reflectivity of gold (a collection optic and a gold-coated diffraction gratings) is calculated using a commercial software package (XCAL, Oxford Research Group). Second, the wavelength-dependent efficiency of a balzed diffraction grating is calculated [see, for instance, Anne P. Thorpe, *Spectrosphysics* (Chapman and Hall, London, 1988)]. Finally, the detection efficiency of the microchannel plate detector is taken from experimental data [O. H. W. Siegmund (unpublished)].

[13] M. H. Key and R. J. Hutcheon, Adv. At. Mol. Phys. **16**, 201 (1980).

[14] M. Domke *et al.*, Phys. Rev. Lett. **66**, 1306 (1991); E. U.

Condon and G. H. Shortley, *The Theory of Atomic Spectra* (Cambridge University Press, Cambridge, 1957).
[15] U. Mohideen *et al.*, Phys. Rev. Lett. **71**, 509 (1993); Eric Mevel *et al.*, *ibid.* **70**, 406 (1993); U. Mohideen, Ph.D. thesis, Columbia University, 1993 (unpublished).
[16] M. V. Ammosov *et al.*, Zh. Eksp. Teor. Fiz. **xx**, xxx (19xx) [Sov. Phys. JETP **64**, 1191 (1986)].
[17] T. Ditmire, Phys. Rev. E **54**, 6735 (1996).
[18] K. A. Janulewicz, M. J. Grout, and G. J. Pert, J. Phys. B **29**, 901 (1996); K. A. Janulewicz, S. B. Healy, and G. J. Pert, Opt. Commun. **130**, 63 (1996).
[19] L. V. Keldysh, Sov. Phys. JETP **20**, 1307 (1965).
[20] P. H. Bucksbaum *et al.*, J. Opt. Soc. Am. B **4**, 760 (1987); R. R. Freeman *et al.*, Phys. Rev. Lett. **59**, 1092 (1987).
[21] P. Pulsifer *et al.*, Phys. Rev. A **49**, 3958 (1994).
[22] F. F. Chen, *Introduction To Plasma Physics and Controlled Fusion* (Plenum, New York, 1990).
[23] R. W. Lee (unpublished). The code FLY can be obtained by contacting R. W. Lee.
[24] G. J. Pert, J. Phys. B **9**, 18 (1976).
[25] L. Vriens and A. Smeets, Phys. Rev. A **22**, 940 (1980).
[26] R. D. Jones and K. Lee, Phys. Fluids **25**, 2307 (1982).
[27] F. G. Patterson, R. Gonzales, and M. D. Perry, Opt. Lett. **16**, 1107 (1991).
[28] M. D. Perry *et al.*, Opt. Lett. **17**, 7 (1992).
[29] J. K. Crane *et al.*, J. Opt. Soc. Am. B **13**, 89 (1996).
[30] W. Kruer, *The Physics of Laser Plasma Interactions* (Addison-Wesley, Reading, MA, 1988).
[31] Lyman Spitzer, *Physics of Fully Ionized Gases* (Interscience, New York, 1956).
[32] A. R. Bell *et al.*, Phys. Rev. Lett. **46**, 243 (1971); F. Malone *et al.*, *ibid.* **34**, 721 (1975); Amiranoff *et al.*, *ibid.* **43**, 522 (1979).
[33] T. E. Glover *et al.*, Phys. Rev. Lett. **76**, 2468 (1996); J. M. Schins *et al.*, *ibid.* **73**, 2180 (1994).